applied sciences

MDPI

Article

Negative Poisson's Ratio Lattice Structure with Chiral and Re-Entrant Properties

Yifei Luo [1], Fulun Dai [2], Jing Shen [3], Aiqiu Wang [1], Xiongzhi Jiang [1] and Yangbo Li [1,*]

[1] College of Hydraulic and Environmental Engineering, China Three Gorges University, Yichang 443002, China
[2] Three Gorges Group China Huashui Hydropower Development Co., Ltd., Chengdu 610041, China
[3] School of Transportation Science and Engineering, Beihang University, Beijing 100191, China
* Correspondence: liyangbo@ctgu.edu.cn

Abstract: Materials exhibiting negative Poisson's ratio (NPR) effects possess several advantageous properties, including high specific strength, specific stiffness, and impact resistance. As a result, they hold significant importance in various industries such as aerospace, medicine, transportation, sports, and other related fields. In the realm of natural materials, the NPR effect is infrequent. Consequently, the creation of an NPR structure necessitates a manual design. In this paper, we present an architected lattice system inspired by ancient Chinese window grills. The proposed system exhibits a unique combination of chiral and re-entrant properties. Experiments and numerical simulations were conducted in order to quantify the variation in NPR and elucidate the deformation mechanism of window grill structures. We observed a significant NPR effect in our designed structure, which was found to be dependent on the geometric parameters of the structure. The present study provides a foundation for the development of a new category of partially auxetic lattice metamaterials and the expansion of their design possibilities.

Keywords: mechanical metamaterial; negative Poisson's ratio; finite element analysis; tensile test

Citation: Luo, Y.; Dai, F.; Shen, J.; Wang, A.; Jiang, X.; Li, Y. Negative Poisson's Ratio Lattice Structure with Chiral and Re-Entrant Properties. *Appl. Sci.* **2023**, *13*, 13097. https://doi.org/10.3390/app132413097

Academic Editor: Marek Krawczuk

Received: 19 October 2023
Revised: 1 December 2023
Accepted: 4 December 2023
Published: 8 December 2023

1. Introduction

With the advancement of contemporary engineering technology, there is a growing need for materials that possess specialized functionalities. However, specialized materials are not readily available in nature. Therefore, the challenge lies in the logical design of artificial microstructure metamaterials that possess advanced physical and mechanical properties. In recent years, there has been a significant increase in the design of mechanical metamaterials with both two- and three-dimensional structures. These designs have been inspired by biological characteristics and macrostructures [1–6]. As a result, these metamaterials exhibit a wide range of functional characteristics [7–15] and have the potential to be applied in various fields. For instance, structures can be designed to obtain materials with a negative Poisson's ratio (NPR). NPR materials have been specifically engineered to possess several notable mechanical properties, including improved resistance to in-plane indentation, increased fracture toughness, an elevated transverse shear modulus, and enhanced dynamic performance. Hence, these materials possess significant potential for applications in medical devices, sports engineering, shock absorption, and the aerospace industry.

In 1985, Almgren [16] made an attempt to establish structures with an NPR theoretically by utilizing the ideal structures of rods, hinges, and springs. In the same year, Kolpakov [17] introduced a novel method that could be utilized for calculating the NPR of a structure. In 1991, Evans [18] called materials with an NPR by the name "auxetics". Then, the classification of auxetic was introduced by Ting [19] and Branka [20]. NPR materials have been found to exhibit distinct mechanical properties that deviate from those of conventional materials, leading to significant interest in them among researchers [21,22]. For instance, Cardoso [23] conducted an analysis on the occurrence of coupled NPR and the

negative coefficient of thermal expansion. Zhang [24] conducted an analysis on the energy absorption properties of NPR materials. The properties of NPR materials primarily rely on the structural system designs. However, there are also alternative mechanisms that result in a negative Poisson's ratio [25–34]. Numerous studies have been undertaken to investigate the effects of various NPR topologies [35–42]. The two primary structures observed in NPR materials are the re-entrant topology [43–45] and the chiral topology [46–48].

In recent years, there has been a surge in the proposal of different types of two-dimensional and three-dimensional chiral auxetic materials. These designs capitalize on the displacement and ligament bending deformation characteristics exhibited by chiral components. Wojciechowski [25] demonstrated the existence of a negative Poisson's ratio within a chiral and elastically isotropic phase of a thermodynamic model at the molecular level. And, he successfully solved a specific category of chiral and elastically isotropic molecular models at absolute zero temperature, thereby demonstrating the existence of a negative Poisson's ratio [49]. The author also later discussed the role of the center of symmetry in planar models of auxetics [50]. Lakes et al. [51] introduced the concept of six-fold chiral negative Poisson's ratio structures and conducted an investigation into their mechanical properties using a linear elastic model. Alderson et al. [52] proposed designs for four-fold chiral, anti-four-fold chiral, three-fold chiral, and anti-three-fold chiral structures with a negative Poisson's ratio.

In addition to the conventional unit designs, various researchers have put forth innovative metamaterials that exhibit local chiral deformation characteristics. For instance, a two-phase anti-four-chiral structure with an adjustable Poisson's ratio and optimized mechanical performance was designed using a bandgap penalization method [53]. Additionally, a multi-material chiral mechanical metamaterial exhibiting the most optimal negative Poisson's ratio and stiffness was synthesized through the integration of a point-wise smart interpolation model and a bimaterial interpolation method [54]. Furthermore, the advancement of 3D printing technology has opened up new avenues for the production of three-dimensional chiral materials. Jiang et al. [55] introduced structures exhibiting a significant negative Poisson's ratio effect when subjected to large deformation conditions through the utilization of multi-material 3D printing technology. Mizzi et al. [56] have also proposed the fabrication of star-shaped perforated chiral metamaterials using 3D printing technology.

The investigation of re-entrant structures primarily centers around the dynamics of impact, which can be ascribed to the symmetry and lattice properties inherent in these structures. These characteristics render re-entrant structures more efficient in withstanding impact forces. Yu et al. [7] introduced a novel foam-filled two-dimensional negative Poisson's ratio concave hexagonal honeycomb structure that exhibits a high specific energy absorption capacity. Chen et al. [57] successfully enhanced the rigidity of a stretch-dominated lattice by incorporating reinforcing ribs that were oriented perpendicular to the concave direction within conventional stretching unit cells. Saxena [58] conducted an investigation on the properties of negative thermal expansion in concave triangular cell structures made from two distinct materials, highlighting their potential advantages in the field of composite materials. Xiao [59] conducted a comprehensive investigation into the alterations in negative Poisson's ratio observed in honeycomb structure materials when subjected to dynamic compression conditions.

Inspired by the architectural design of ancient Chinese window grills, we have proposed a lattice structure that integrates both chirality and re-entrant characteristics. The structures investigated in this paper pertain to the anti-four-fold chiral class of structures, and there exists a multitude of structures that fall within this classification. For instance, Pozniak [60] conducted an investigation on the influence of disorder in anti-chiral rectangular structures using the finite element method (FEM). Strek [61] conducted a study on the significant deformations of a structure that bears resemblance to those discussed in this paper, utilizing the finite element method (FEM). Tabacu [62] conducted a comprehensive analysis to investigate anti-tetra-chiral structures. There have been studies conducted on

the molecular level regarding tetra-chiral auxetic systems that exhibit similarities [63–65]. Furthermore, Lim conducted a comprehensive investigation into different auxetic structures that are derived from ancient geometrical patterns [66,67]. In addition, Hoover and Hoover examined intricate mechanisms of auxeticity [30]. Last but not least, it has been observed that certain cooperative mechanisms exist in axial 3D models of many-body systems that exhibit square symmetry in the plane perpendicular to the axis. For instance, Narojczyk studied the purely geometric models of atomic auxetic systems [68] and auxetics with molecular inclusions [69].

In the present study, the utilization of static tensile tests and finite element numerical simulation analysis allowed for the quantification of variations in NPR and the elucidation of the deformation mechanism of lattice structures. The structure exhibited a significant NPR effect, and the magnitude of this effect was dependent on the geometric parameters. This study aims to extend the existing research model of NPR structures, thereby establishing a robust foundation for examining the performance of chiral and re-entrant NPR structures.

2. Structural Design and Methods

2.1. Unit Cell Design

Based on the geometric characteristics of traditional Chinese window grills, a lattice metamaterial was developed that demonstrated re-entrant and chiral properties. The structure depicted in Figure 1b was derived from the design of the traditional Chinese window grill illustrated in Figure 1a. The unit cell depicted in Figure 1c was derived through the process of duplicating, rotating, and reflecting the quarter unit cell. The lattice materials depicted in Figure 1d were acquired through the arrangement of the unit cell.

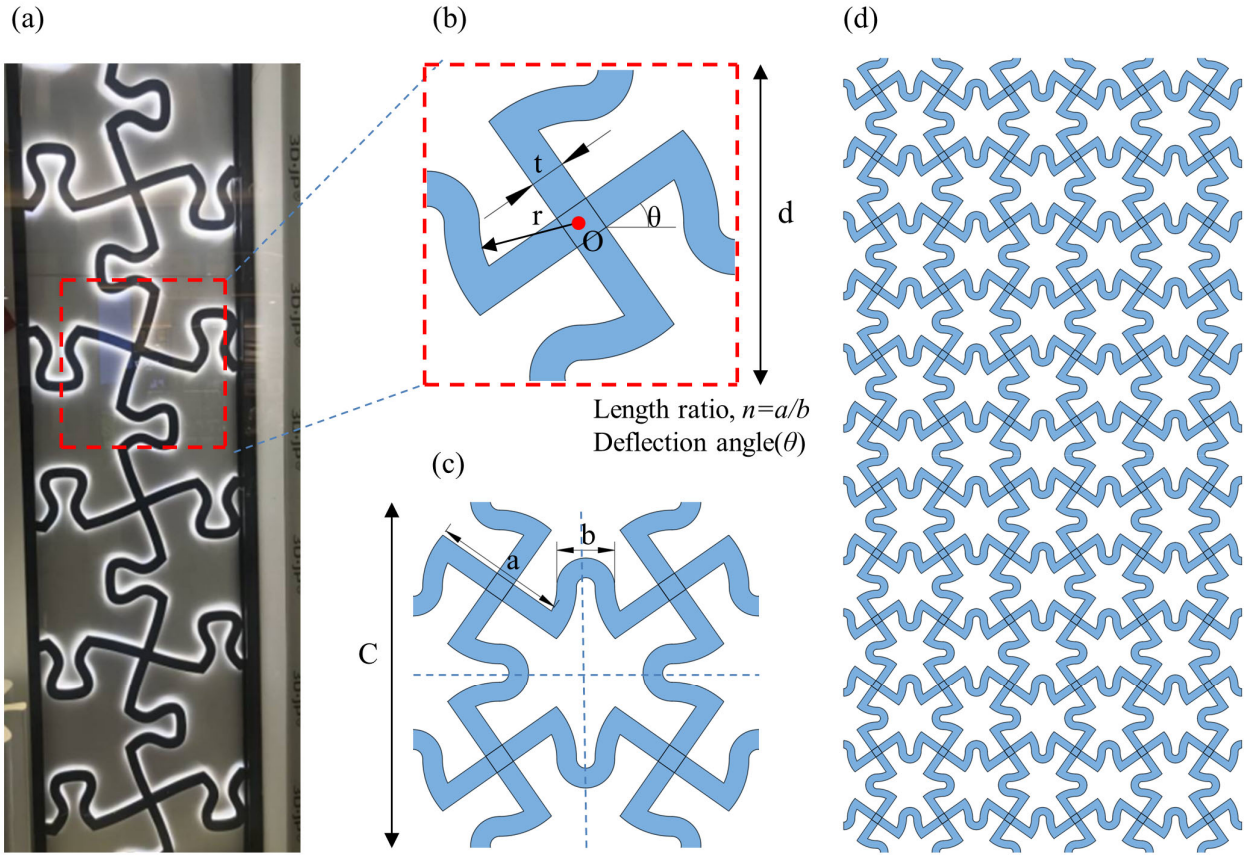

Figure 1. Structure of window grills (**a**), design of quarter unit cell (**b**), design of unit cell (**c**), the lattice metamaterial (**d**).

The geometrical parameters of the unit cell are shown in Figures 1 and 2. In this study, a is the length of the chiral cross, b is the diameter of the re-entrant circle, C is the unit cell length, d is the side length of a quarter unit cell, t is the thickness of the chiral cross or re-entrant circle, θ is the chiral cross deflection angle, and r is the arc radius connecting the cross structure and the concave structure. The C and t are constant values, which were 52 mm and 3 mm, respectively. The relationship of some parameters can be expressed as follows:

$$C = 2\mathrm{d} \tag{1}$$

$$\mathrm{r} = \frac{a}{2} - t \tag{2}$$

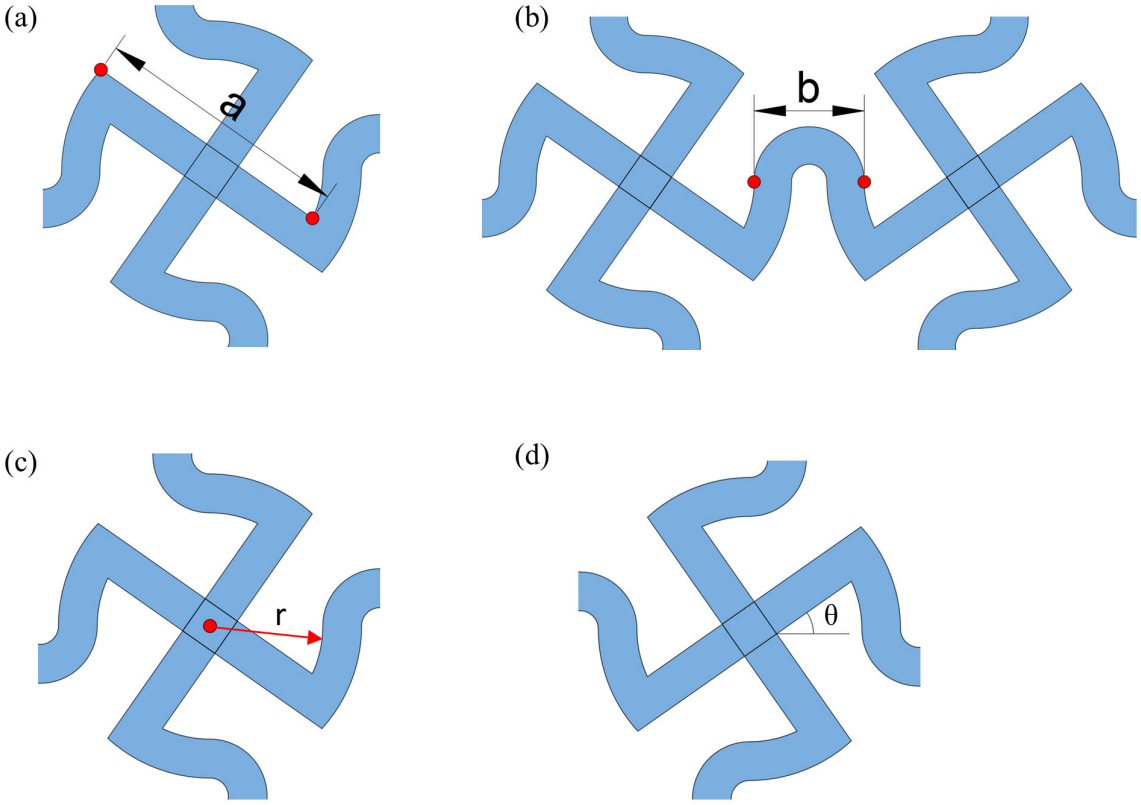

Figure 2. The schematic diagram of geometric parameters: the length of the chiral cross a (**a**), the diameter of the re-entrant circle b (**b**), the arc radius connecting the cross structure and the concave structure r (**c**) and the deflection angle θ (**d**).

Because of the fixed total length of the quarter unit cell d, an increase in a leads to a decrease in b. Therefore, we defined the length ratio (a/b) and the deflection angle (θ) as the independent variables of structural geometric parameters. a is the length of the cross and b is the diameter of the concave arc. The two are connected by an arc with a radius of r and a center angle of θ.

Thus, 4 independent parameters are defined in this study. They are length ratio (a/b), deflection angle (θ), unit cell length (C), and the thickness of the chiral cross or re-entrant circle (t). After defining the geometrical parameters and their relationships, we could explore the influences of changes in structural geometrical parameters on NPR.

2.2. Design of Re-Entrant and Chiral Structures

To investigate the influence of geometric parameters on NPR, this study incorporated the length ratio (a/b) and the deflection angle (θ) as variables that represented the structural geometric parameters.

To examine the influence of geometric parameters on the NPR phenomenon in a structure, a comprehensive set of 90 unique models, consisting of re-entrant and chiral lattice structures, were generated specifically for finite element numerical simulation. The NPR of typical representative units (as shown in Figure 3) was observed and subsequently subjected to comparison. The transverse representation is employed to illustrate structural components at different deflection angles (θ) ranging from 0° to 45°, including increments of 5° (i.e., 0°, 5°, 10°, 15°, 20°, 25°, 30°, 35°, 40°, and 45°). On the other hand, the utilization of the vertical representation is employed to visually depict the various structural units at distinct length ratios, such as 0.237, 0.343, 0.621, 0.810, 1.046, 1.771, 2.367, 3.290, and 7.202.

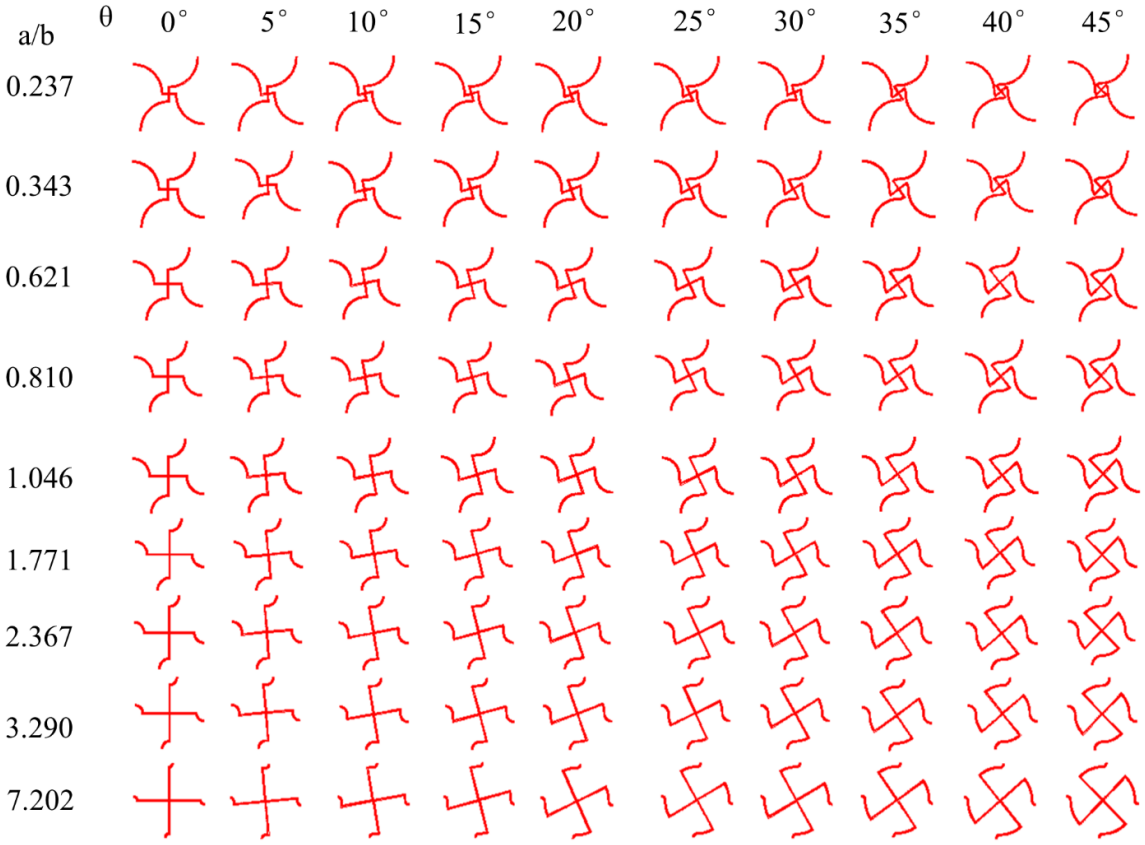

Figure 3. Quarter structure unit consisting of different length ratios (*a/b*) and deflection angle (θ).

2.3. Model Production

We used a 3D printer utilizing stereolithography appearance (SLA) technology to manufacture the specimens. The printer can be seen in Figure 4b. The primary benefit of this technology lies in its ability to produce printed specimens with a high level of accuracy. The principle underlying SLA technology involves the rapid curing of a liquid photosensitive resin to form a solid structure when exposed to laser or UV irradiation (Figure 4a).

The fabrication process could be divided into two distinct steps. First and foremost, the utilization of software was employed to conduct computer-based modeling of samples. The process involved converting the three-dimensional model into a series of two-dimensional images using slicing software. Secondly, the sliced images were subsequently transmitted to the printing platform, where the photosensitive resin underwent curing into the shape depicted in the sliced image through the process of UV irradiation. The aforementioned procedure was iteratively executed, with each layer being added successively, until the entire model was fully constructed.

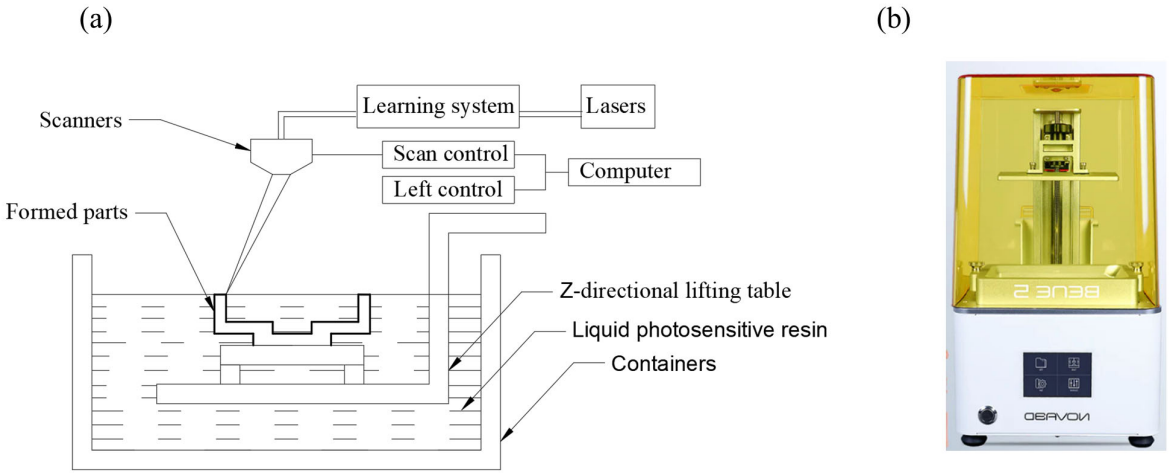

Figure 4. The principle of the SLA printing process (**a**) and the 3D printer (**b**).

2.4. The Material Parameter of Samples

Through 3D printing, the dog bone samples were fabricated as shown in Figure 5a. Static tensile tests were performed using a university testing machine (FBS-HW10KNW) at room temperature, according to the standard GB/T1040-79. The loading speed was 5 mm/min. Figure 5b shows the stress–strain curves of the samples. The other material parameters of elasticity modulus, Poisson's ratio, and density were E = 2.51 GPa, γ = 0.41, and $\rho = 1.774 \times 10^3 \mathrm{kg/m}^3$.

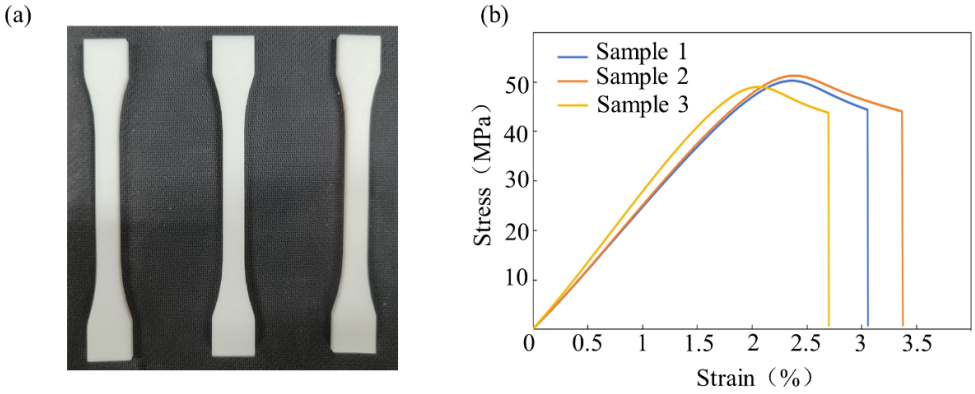

Figure 5. The dog bone samples for the tensile test (**a**) and the stress–strain curve of specimens obtained by tensile test (**b**).

2.5. Experimental Tests

To investigate the negative Poisson's ratio phenomenon in the window grill structure, we opted for a specific structure with a length ratio (a/b) of 2.367 and a deflection angle (θ) of 35 for both sample printing and experimental analysis. The sample had a longitudinal arrangement of 6 unit cells and a lateral arrangement of 3 unit cells, as depicted in Figure 6a. Additionally, the thickness of the chiral cross or re-entrant circle was t = 3 mm and the angle of inclination was $\theta = 35°$. The thickness of the lattice metamaterial measured 10 mm.

The experiment utilized a CMT410G microcomputer-controlled electronic universal testing machine and an OSG030-815UM high-speed camera with a resolution of 5 million pixels. The experimental procedure is depicted in Figure 6b.

First, the upper and lower fixtures were utilized to securely fasten the two ends of the specimen, as depicted in the section highlighted in Figure 6a. The distance between the upper and lower fixtures were adjusted in accordance with the standard GB/T 1040-79. The proper clamping of the test specimen for the window structure was of the utmost importance. It was imperative to maintain the vertical orientation of the specimen to

prevent any occurrence of bending deformation during the testing procedure. Proper maintenance of the distance between the fixture and the end of the specimen was crucial to prevent fracture at the end caused by concentrated local stress.

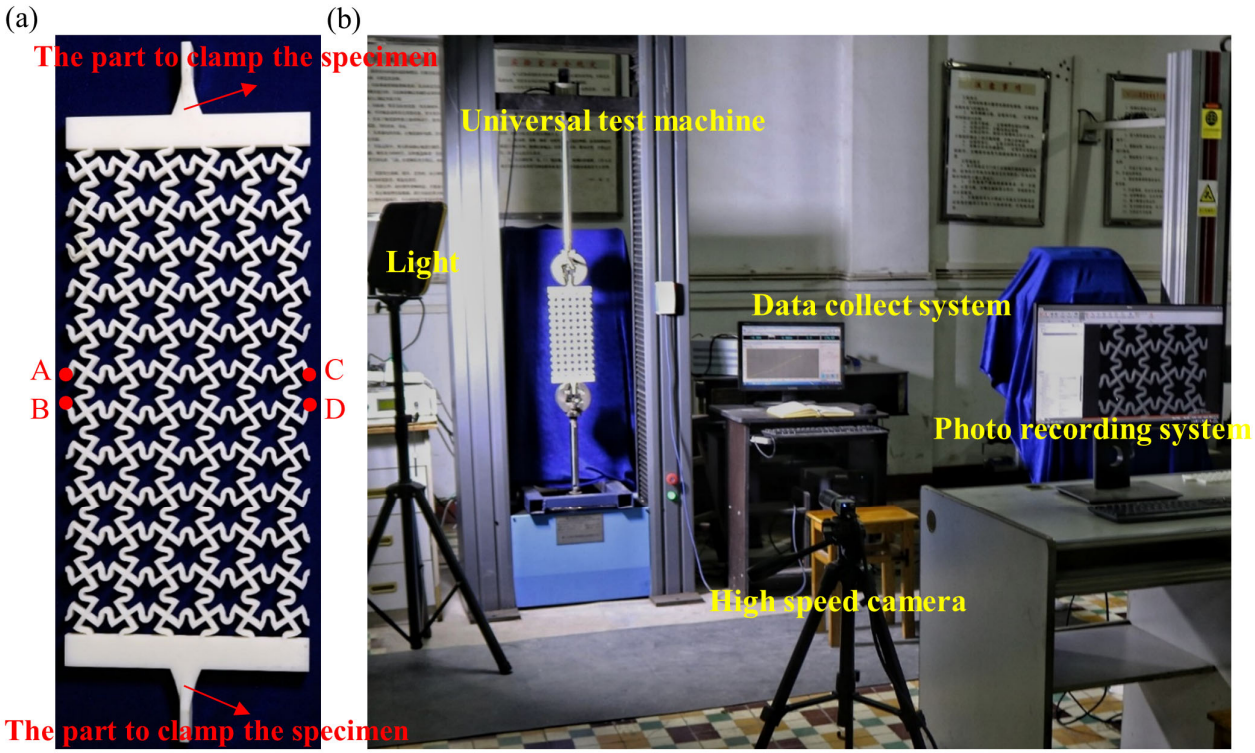

Figure 6. (**a**) Schematic diagram of the measurement point and (**b**) the experiment process.

Secondly, in this experimental setup, the lower end of the test piece remained fixed, while the upper end was subjected to a tensile force. The tensile speed for the applied load was set at 2 mm/min. The test was terminated at various points when the tensile load reached 600, 700, 800, 900, 1000, 1100, and 1200 N.

Thirdly, the utilization of a high-speed camera enabled the capturing of images at a frequency of 0.2 s during the static tensile experiment. According to the Saint-Venant principle, the stress experienced by an elastomer located far from a load action zone is solely determined by the combined force acting on it.

To isolate the impact of the load on the NPR, we specifically chose the central region of the specimen as the designated calculation area. The displacement alterations of four distinct points (A, B, C, and D) as depicted in Figure 6a were measured. The NPR could be determined by utilizing formulas 3 to 5.

2.6. Finite Element Analysis

The static simulation was performed using the commercially available software ANSYS 14.0. First, a model was created with identical dimensional and material parameters, as described in Section 2.3 regarding the specimens. In the simulation of the static tensile test, the fixed constraints were applied to the bottom of the ancient window grill system, while the upper end of the test piece was subjected to the same loading conditions as outlined in Section 2.4. The schematic diagram is depicted in Figure 7a.

Secondly, it was important to maintain consistent boundary and loading conditions while employing finite element techniques to analyze the negative Poisson's ratios of 90 distinct structures, as depicted in Figure 3. The objective of this study was to examine the impact of geometric parameters on the negative Poisson's ratio values and understand how changes in these parameters influenced the mechanical behavior of the structures.

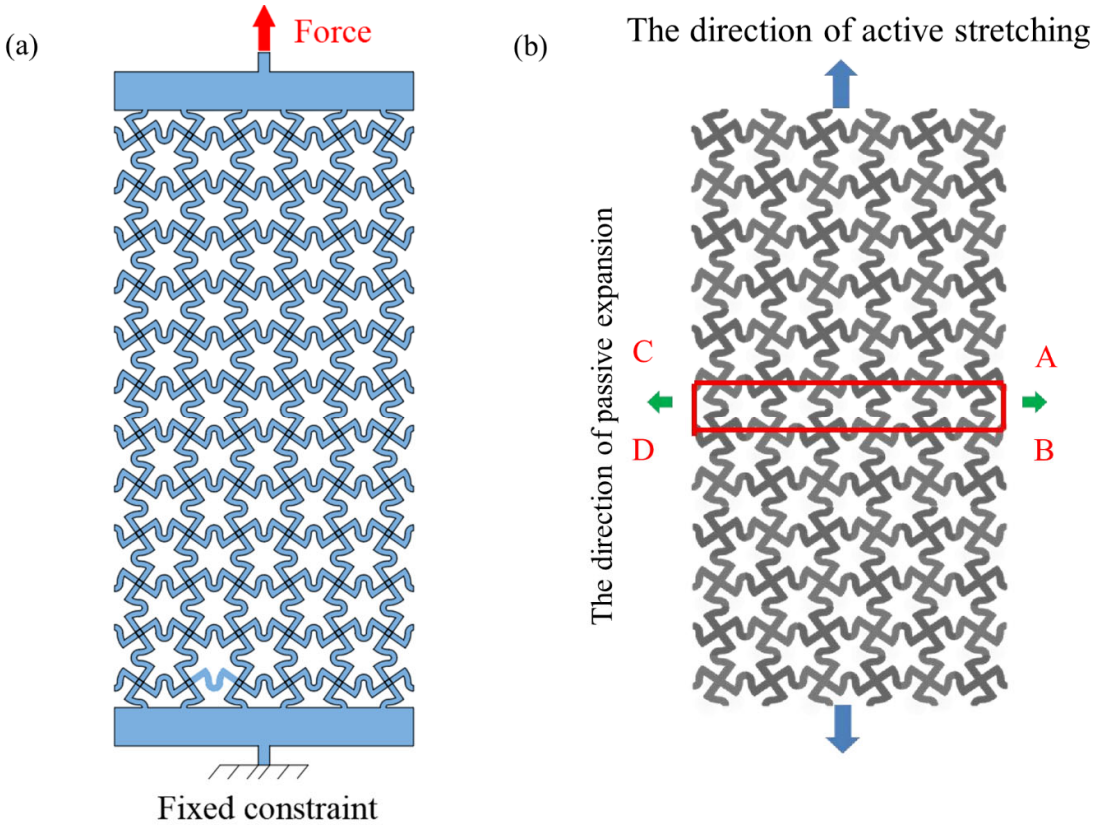

Figure 7. Schematic of the simulation (**a**) and calculation of Poisson's ratio (**b**).

The numerical simulation of the window grill structure fell under the category of thin plate bending problems, primarily due to its dot matrix structure which exhibited a high level of regularity. Thus, the element utilized for meshing was plane-182, which fell under the category of linear elements.

To exclusively examine the impact of load on the NPR, we opted to analyze the central region of the specimen as the designated calculation area (see Figure 7b). The blue arrow symbolizes the direction of active stretching, while the green arrow represents the direction of passive expansion. The red box denotes the calculation area for the NPR. To minimize potential errors, we performed calculations for two Poisson's ratios and subsequently obtained their average value. The calculation process can be outlined as follows:

$$v_1 = -\frac{\varepsilon_1'}{\varepsilon_1} = -\frac{\frac{\Delta AC}{AC}}{\frac{\Delta AB}{AB}} \tag{3}$$

$$v_2 = -\frac{\varepsilon_2'}{\varepsilon_2} = -\frac{\frac{\Delta BD}{BD}}{\frac{\Delta CD}{CD}} \tag{4}$$

$$v = \frac{v_1 + v_2}{2} \tag{5}$$

when utilizing ANSYS software to analyze stress and strain in the stretching process, it was observed that a finer mesh division led to more precise calculation results. However, once the grid had been divided to a certain extent, additional division had a minimal effect on the outcomes.

In order to mitigate the occurrence of redundant and erroneous calculation durations, we consulted the research conducted by Pozniak et al. [33] and imposed a constraint on the maximum length of the segment, denoted as dmax. The dependence of the result on the mesh was plotted, as depicted in Figure 8b. The findings suggested that the influence on the negative Poisson's ratio was not substantial when the grid length ranged from 0.5

to 3. In order to ensure the precision of the outcomes and minimize the utilization of computational resources, the maximum length of the element edge (dmax) was established at 1.5.

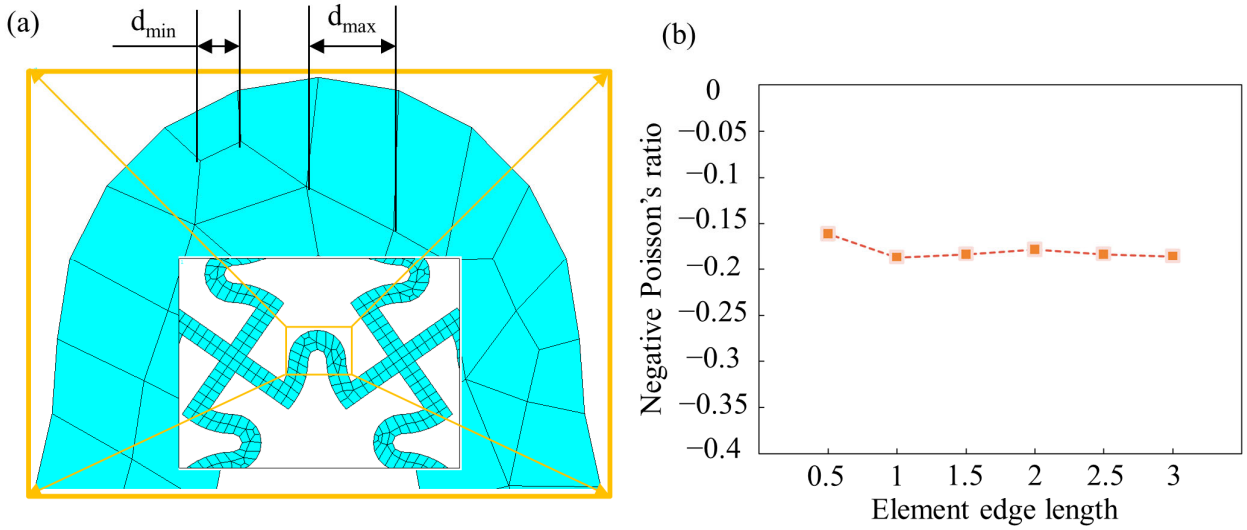

Figure 8. The schematic diagram of mesh (**a**) and the dependence of negative Poisson's ratio on the mesh (**b**).

3. Results and Discussions

3.1. Experiment Result

The deformation process of the unit cell in the specimen, captured by a high-speed camera prior to and following tension, is depicted in Figure 9a. The observed transverse expansion in the cell could be attributed to the longitudinal stretching, which indicated the manifestation of an NPR effect in the designed window grill structure. Furthermore, Figure 9b demonstrates that despite the fluctuation in the maximum tensile force of the specimen, the NPR value remained consistently constant. The structural nature of the NPR was primarily characterized by its independence from material or load factors. Manifestations of NPR generally entailed the manipulation of a structure through processes such as folding, rotating, or bending. An augmentation in longitudinal tension led to a corresponding increase in transverse expansion, consequently causing a modification in the NPR of the structure.

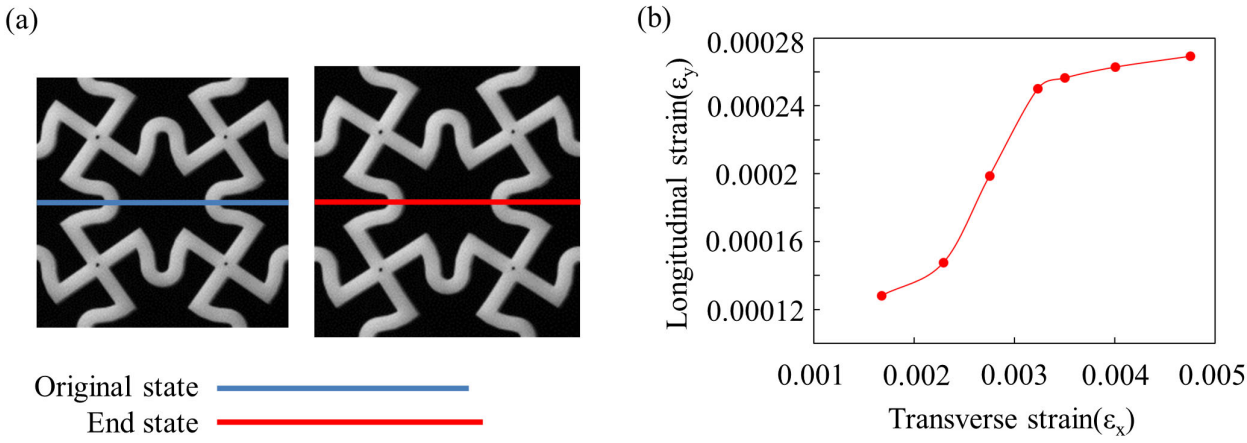

Figure 9. Comparison of the original and end states of the tensile specimen (**a**) and the experiment result (**b**).

3.2. Finite Element Numerical Simulation Result

Figure 10a,b depict the longitudinal and transverse displacement diagrams acquired through finite element analysis. When the specimen underwent longitudinal tension, it experienced transverse expansion, leading to the occurrence of an NPR effect. The outcomes of this numerical simulation exhibited congruity with the findings of the experimental study.

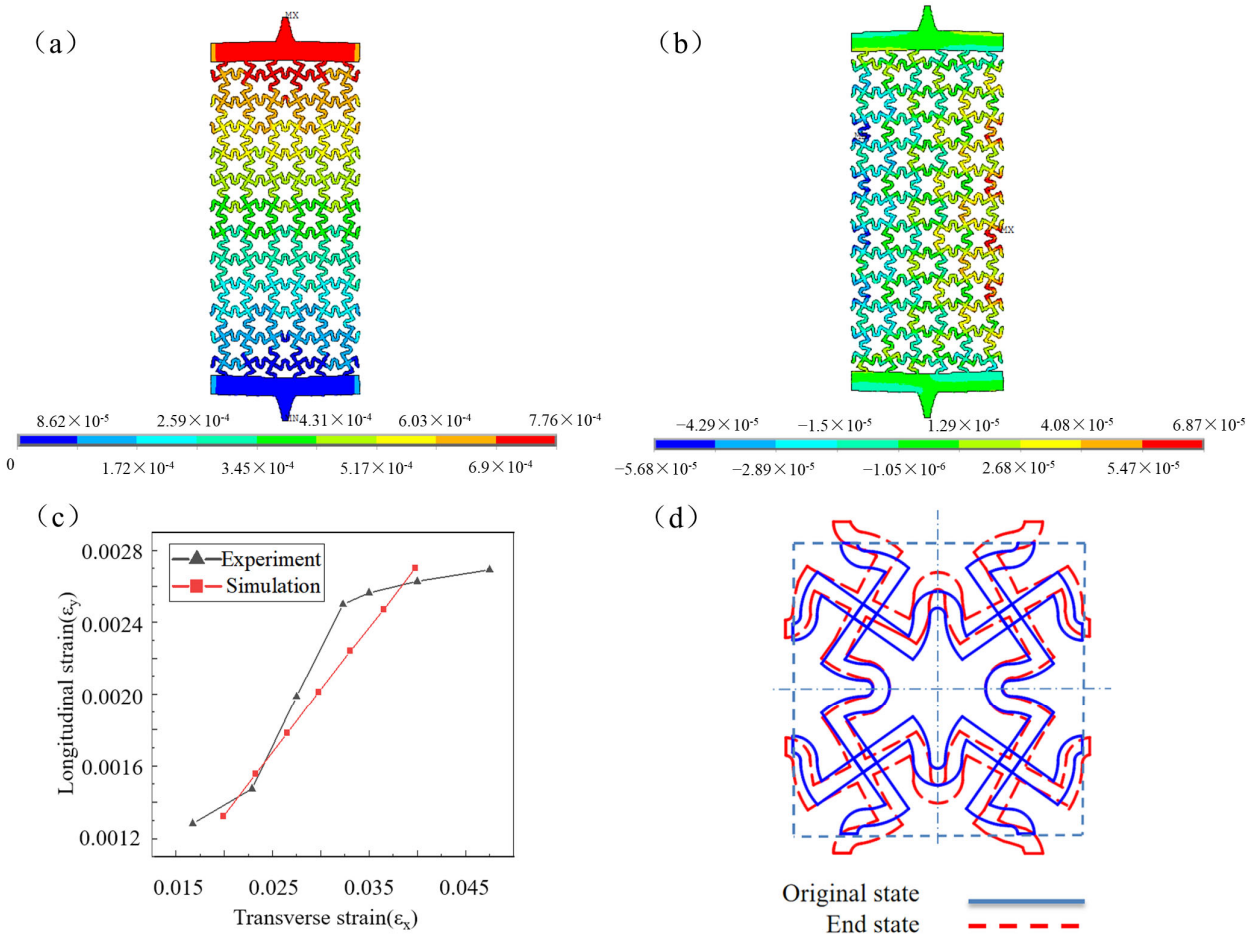

Figure 10. The cloud picture of y-direction (**a**) and x-direction (**b**), the comparison between the experiment and the simulation (**c**), and the deformation process of the window grill structure (**d**).

Figure 10c displays the outcomes of the static tensile experiments and finite element simulations, with the inclination of the curve indicating the Poisson's ratio. The simulation exhibited a negative Poisson's ratio of −0.09, whereas the experimental average negative Poisson's ratio was −0.07. The results obtained from the experiment and the simulation exhibited a high degree of similarity, thereby providing substantial evidence for the accuracy of the finite element simulation discussed in Section 3.4. It was observed that the strain–strain dependence in the experimental data was non-linear, in contrast to the linear dependence observed in the simulations. The presence of human error, experimental instrument error, and other factors during the experimental process can account for this phenomenon.

In addition, we conducted an examination of the structure of individual cells while considering the effects of periodic boundary conditions. The lattice structure of an 8 × 8 unit cell was analyzed under identical boundary conditions and loads as the original lattice structure. The negative Poisson's ratio in the central region, as depicted in Figure 11a, was determined using the same methodology outlined in Section 2.5. The results of the calculations are presented in Figure 11b. The slope depicted in the figure indicates a negative Poisson's ratio, and our analysis revealed that the negative Poisson's ratios of the

two samples were closely aligned. However, under periodic conditions, the single-cell structure exhibited reduced stress and strain changes when subjected to the same load, which could be attributed to the larger scale of the lattice structure.

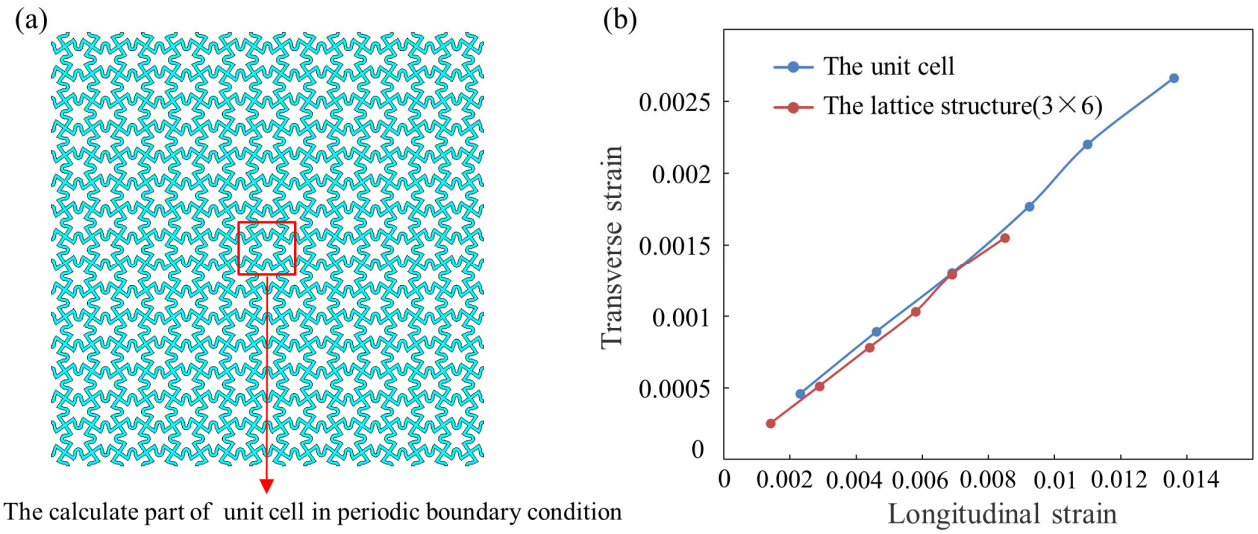

Figure 11. The schematic diagram of a unit cell in periodic boundary conditions (**a**) and the result between the unit cell and the 3 × 6 unit cell structure (**b**).

3.3. The Deformation Mechanism

In order to enhance the observation of the deformation mechanism of the model, this study employed the zoom-in feature of Ansys software to amplify the results of the numerical simulation analysis by a factor of 30,000. The central unit cell of the overall lattice structure was then selected for detailed observation and analysis. In order to effectively illustrate the alterations in displacement resulting from structural stretching, the outcomes of the numerical simulation for stretching were extracted and imported into AutoCAD for data manipulation. The original unit cell and the stretched unit cell were overlaid in order to visualize the deformation, as depicted in Figure 10d.

The comparison and analysis of the deformation process were conducted for both the pre-stretching and post-stretching stages of the specimen. When a uniaxial force was exerted in the vertical direction on the model, the entire structure exhibited simultaneous expansion in both the horizontal and vertical dimensions. The active bar units were defined as the bar units aligned with the direction of tension, whereas the passive bar units were those orthogonal to the load direction. Due to the constraints imposed by the neighboring bar unit cells, the stimulated bar units exhibited vertical mobility, whereas the passive bar units exhibited horizontal mobility. The extent of deformation in the rod element was assessed based on the angular displacement between the rods, which progressively increased as the structure experienced expansion due to tension. Variations in the deformation of the angle between the active and passive rods were observed. In chiral bar unit cells, the active bar elements underwent compression or stretching in the vertical direction, resulting in rotational motion and propelling the passive bar elements.

3.4. The Influence of Geometric Parameters on NPR

The findings from Section 3.2 demonstrate a robust correlation between the numerical analysis results and the experimental findings. In order to conduct an analysis on the influence of geometric parameters on NPR, we chose the side length of the chiral cross (a), outer diameter of the re-entrant structure (b), and (θ) as the variables, as depicted in Figure 1. However, due to the constant overall length of the individual cell, the value of b varied as a increased. Therefore, the a/b ratio, also known as the length ratio, and the deflection angle (θ) were designated as the variables representing the structural geometric

parameters. The application of numerical analysis techniques facilitated the computation of negative values for Poisson's ratios.

The results of the finite element numerical simulations for the NPRs of the window grill lattice structures are presented in Figure 12. The simulations were conducted for combinations of nine different length ratios (*a*/*b*) and ten deflection angles (θ). Figure 12a depicts the variation in the NPR of a window grill lattice structure with an increasing deflection angle (θ) and constant length ratio. As the deflection angle (θ) increased, the influence of NPR tended to diminish. The observed decrease in strength could be ascribed to the constriction of the expansion area of the re-entrant structure when exposed to longitudinal static stretching at higher deflection angles. As a consequence, the application of compression mitigated the horizontal expansion phenomenon of the structure on a macroscopic scale. Consequently, as the deflection angle (θ) increased, the presence of the re-entrant structure led to a weakening of the NPR effect.

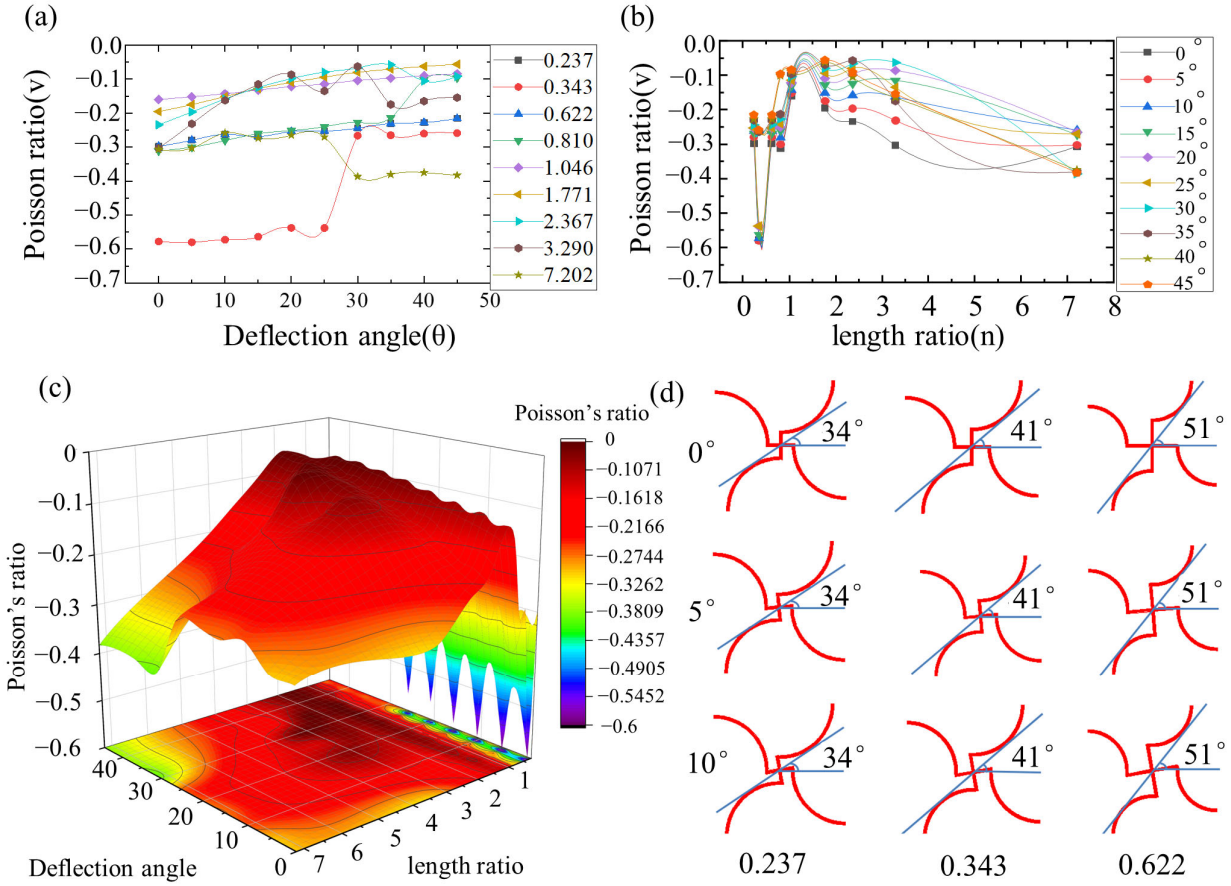

Figure 12. Structural design model of the evolution of the NPR at different deflection angles (**a**) and different length ratios (**b**), the 3D (a/b)-(θ)-(PR) plot (**c**), and a schematic diagram of the re-entrant chiral deflection angle (**d**).

When the length ratio (*a*/*b*) fell within the range of 3.290 to 7.202 and the deflection angle (θ) exceeded 30°, the NPR effect was observed to be enhanced. This enhancement could be attributed to the presence of the largest geometric dimensions in the chiral structure and the smallest geometric dimensions in the re-entrant structure. As the deflection angle (θ) increased, the re-entrant structure underwent further compression, resulting in a reduction in its geometric size. Consequently, the chiral structure played a crucial role in the non-planar re-entrant effect, thereby promoting the overall effect.

It was observed that the NPR effect increased when the length ratio (*a*/*b*) was 0.343 and the deflection angles (θ) ranged from 0° to 25°. The observed outcome could be ascribed to the specific configuration of the chiral cross structure. To offer a comprehensive

elucidation of this matter, this article delineates the concave chiral deflection angle, as illustrated in Figure 11d. When the length ratio was 0.343, the re-entrant chiral deflection angle approached 41°, which was the value closest to 45°. This phenomenon amplified the adverse Poisson's effect on the structure. Additionally, the deflection angle did not impede the range of the concave chiral torsion angle, which spanned from 0 to 25°.

Figure 12b illustrates the variation of the NPR effect as the length ratio (*a/b*) increased while the deflection angle (θ) was constant. As the length ratio (a/b) increased, the NPR effect exhibited a sharp increase followed by a sharp decrease and gradual increase. The influence of the change in the length ratio (*a/b*) on the NPR effect was found to be greater than that of the deflection angle.

Through the finite element analysis results (see Figure 12), it was determined that the lattice structure of the ancient Chinese window grill demonstrated an NPR effect when exposed to static tension. When the length ratio (*a/b*) was 0.343 and the deflection angle (θ) ranged from 0° to 20°, the structure exhibited its maximum NPR effect, with an NPR value of approximately −0.6. At the same time, it could be inferred that the impact of the deflection angle on the negative Poisson's ratio of the structure followed a gradual trajectory, whereas the influence of the length ratio on the negative Poisson's ratio exhibited fluctuations. Particularly when the length ratio fell within the range of 3.5 to 7, irrespective of variations in the angle, the negative Poisson's ratio demonstrated an amplified tendency.

In order to validate the rationality of the numerical simulation findings, we consulted the studies conducted by other researchers and conducted a comparative analysis of the outcomes. One of the structures designed by Gaspar [70], which was similar to the structure of our study, exhibited a negative Poisson's ratio as low as −0.6. This validation substantiates the findings of our research. At the same time, in contrast to prior research, this article provides a more comprehensive analysis of the impact of geometric parameters on the negative Poisson's ratio. It investigates the influence of various deflection angles and length ratios on the negative Poisson's ratio of structures.

4. Conclusions

NPR structures are widely used in aerospace, sports, and medical fields because they are lightweight and have high strength, impact resistance, and seismic resistance. This study proposed a novel NPR structure based on ancient Chinese window grills. The structure combined chiral and re-entrant structures. Static tensile tests were conducted to verify the NPR effect of the structure, and finite element numerical simulation experiments were conducted to study changes in the NPR effect of the structure under changing geometric parameters. The following conclusions were obtained:

1. The ancient Chinese window lattice structure exhibited an NPR effect under static tension.

2. The deformation mechanism was explored. The unit cell rotated when subjected to longitudinal tension and the concave part opened outward under tensile force. The overall structure exhibited outward expansion at the macro level.

3. As the deflection angle increased, the re-entrant structure weakened the NPR effect. As the length ratio increased, the NPR effect increased sharply, decreased sharply, and, finally, slowly increased.

4. The strongest NPR effect of the structure was observed at a length ratio of 0.343 and deflection angles of 0°–20°, and the NPR ratio reached −0.6.

It can be envisioned that the proposed design strategy can be extended to any other structure that combines re-entrant and chiral properties, providing insights into the development of a new class of architected metamaterials with potential applications in construction engineering, sports protection, aerospace, biomedical sensors, and semiconductors. In the next step, we plan to study the low-speed impact resistance of the Chinese ancient window grill structure to explore the energy dissipation characteristics of the NPR structure.

Author Contributions: Y.L. (Yifei Luo) performed the conceptualization, data curation, formal analysis, and investigation. F.D. was responsible for the methodology, validation, and editing. J.S. completed the writing. A.W. conducted the experiments. X.J. provided the experimental platform. Y.L. (Yangbo Li) conceived the idea. All authors have read and agreed to the published version of the manuscript.

Funding: This research received no external funding.

Institutional Review Board Statement: Not applicable.

Informed Consent Statement: Not applicable.

Data Availability Statement: Data are contained within the article.

Acknowledgments: The author appreciates the support of the 3D printing team at China Three Gorges University.

Conflicts of Interest: The authors declare that they have no known competing financial interest or personal relationship that could have appeared to influence the work reported in this paper.

References

1. Wu, W.; Hu, W.; Qian, G.; Liao, H.; Xu, X.; Berto, F. Mechanical design and multifunctional applications of chiral mechanical metamaterials: A review. *Mater. Des.* **2019**, *180*, 107950. [CrossRef]
2. Li, Y.; Shen, Y.; Cao, S.; Zhang, X.; Meng, Y. Thermally triggered tunable vibration mitigation in Hoberman spherical lattice metamaterials. *Appl. Phys. Lett.* **2019**, *114*, 191904. [CrossRef]
3. Xie, Y.B.; Popa, B.I.; Zigoneanu, L.; Cummer, S.A. Measurement of a Broadband Negative Index with Space-Coiling Acoustic Metamaterials. *Phys. Rev. Lett.* **2013**, *110*, 175501. [CrossRef] [PubMed]
4. Zhang, B.H.; Xu, K.D. Switchable and tunable bifunctional THz metamaterial absorber. *J. Opt. Soc. Am. B Opt. Phys.* **2022**, *39*, A52–A60. [CrossRef]
5. Zhang, C.; Cheng, Q.; Yang, J.; Zhao, J.; Cui, T. Broadband metamaterial for optical transparency and microwave absorption. *Appl. Phys. Lett.* **2017**, *110*, 143511. [CrossRef]
6. Zhao, J.; Cheng, Q.; Chen, J.; Qi, M.; Jiang, W.; Cui, T. A tunable metamaterial absorber using varactor diodes. *New J. Phys.* **2013**, *15*, 043049. [CrossRef]
7. Yu, R.; Luo, W.; Yuan, H.; Liu, J.; He, W.; Yu, Z. Experimental and numerical research on foam filled re-entrant cellular structure with negative Poisson's ratio. *Thin-Walled Struct.* **2020**, *153*, 106679. [CrossRef]
8. Li, D.; Gao, R.; Dong, L.; Lam, W.K.; Zhang, F. A novel 3D re-entrant unit cell structure with negative Poisson's ratio and tunable stiffness. *Smart Mater. Struct.* **2020**, *29*, 045015. [CrossRef]
9. Zhang, X.Y.; Ren, X.; Zhang, Y.; Xie, Y.M. A novel auxetic metamaterial with enhanced mechanical properties and tunable auxeticity. *Thin-Walled Struct.* **2022**, *174*, 109162. [CrossRef]
10. Ge, X.Q.; Xiang, H.R.; Liu, Y.; Shen, J.; Li, Y.; Li, Y. Utilizing reversible solid-liquid phase transition to tune phononic bandgaps. *AIP Adv.* **2021**, *11*, 125323. [CrossRef]
11. Lu, Z.Q.; Zhao, L.; Ding, H.; Chen, L.Q. A dual-functional metamaterial for integrated vibration isolation and energy harvesting. *J. Sound Vib.* **2021**, *509*, 116251. [CrossRef]
12. Liu, Y.; Shen, J.; Li, Y.J.; Ge, X.Q.; Li, Y.B. Enhanced high-strain-rate impact resistance of helicoidal composites by fused deposition modelling. *Mech. Adv. Mater. Struct.* **2022**, *29*, 7796–7808. [CrossRef]
13. Lu, X.C.; Zhang, X.M.; Li, Y.B.; Shen, Y.; Ma, Y.Q.; Meng, Y.D. Enhanced Low-Velocity Impact Resistance of Helicoidal Composites by Fused Filament Fabrication (FFF). *Polymers* **2022**, *14*, 1440. [CrossRef]
14. Li, Y.; Chen, Y.; Li, T.; Cao, S.Y.; Wang, L.F. Hoberman-sphere-inspired lattice metamaterials with tunable negative thermal expansion. *Compos. Struct.* **2018**, *189*, 586–597. [CrossRef]
15. Wang, Q.M.; Jackson, J.A.; Ge, Q.; Hopkins, J.B.; Spadaccini, C.M.; Fang, N.X. Lightweight Mechanical Metamaterials with Tunable Negative Thermal Expansion. *Phys. Rev. Lett.* **2016**, *117*, 175901. [CrossRef] [PubMed]
16. Almgren, R.F. An isotropic three-dimensional structure with Poisson's ratio = − 1. *J. Elast* **1985**, *15*, 427–430.
17. Kolpakov, A.G. Determination of the average characteristics of elastic frameworks. *J. Appl. Math. Mech.* **1985**, *49*, 739–745. [CrossRef]
18. Evans, K.E. Auxetic polymers: A new range of materials. *Endeavour* **1991**, *15*, 170–174. [CrossRef]
19. Brańka, A.C.; Heyes, D.M.; Wojciechowski, K.W. Auxeticity of cubic materials. *Phys. Status Solidi (B)* **2009**, *246*, 2063–2071. [CrossRef]
20. Ting, T.C.T.; Barnett, D.M. Negative Poisson's Ratios in Anisotropic Linear Elastic Media. *J. Appl. Mech.* **2005**, *72*, 929–931. [CrossRef]
21. Luo, C.; Han, C.Z.; Zhang, X.Y.; Zhang, X.G.; Ren, X.; Xie, Y.M. Design, manufacturing and applications of auxetic tubular structures: A review. *Thin-Walled Struct.* **2021**, *163*, 107682. [CrossRef]

22. Jiang, W.; Ren, X.; Wang, S.L.; Zhang, X.G.; Zhang, X.Y.; Luo, C.; Xie, Y.M.; Scarpa, F.; Alderson, A.; Evans, K.E. Manufacturing, characteristics and applications of auxetic foams: A state-of-the-art review. *Compos. Part B Eng.* **2022**, *235*, 109733. [CrossRef]
23. Cardoso, J.O.; Borges, J.P.; Velhinho, A. Structural metamaterials with negative mechanical/thermomechanical indices: A review. *Prog. Nat. Sci. Mater. Int.* **2021**, *31*, 801–808. [CrossRef]
24. Zhang, J.; Lu, G.; You, Z. Large deformation and energy absorption of additively manufactured auxetic materials and structures: A review. *Compos. Part B Eng.* **2020**, *201*, 108340. [CrossRef]
25. Wojciechowski, K.W. Constant thermodynamic tension Monte Carlo studies of elastic properties of a two-dimensional system of hard cyclic hexamers. *Mol. Phys.* **1987**, *61*, 1247–1258. [CrossRef]
26. Milton, G.W. Composite materials with poisson's ratios close to −1. *J. Mech. Phys. Solids* **1992**, *40*, 1105–1137. [CrossRef]
27. Baughman, R.H.; Shacklette, J.M.; Zakhidov, A.A.; Stafström, S. Negative Poisson's ratios as a common feature of cubic metals. *Nature* **1998**, *392*, 362–365. [CrossRef]
28. Kimizuka, H.; Kaburaki, H.; Kogure, Y. Mechanism for negative Poisson ratios over the alpha-beta transition of cristobalite, SiO_2: A molecular-dynamics study. *Phys. Rev. Lett.* **2000**, *84*, 5548–5551. [CrossRef]
29. Tretiakov, K.V.; Wojciechowski, K.W. Poisson's ratio of simple planar 'isotropic' solids in two dimensions. *Phys. Status Solidi (B)* **2007**, *244*, 1038–1046. [CrossRef]
30. Hoover, W.G.; Hoover, C.G. Searching for auxetics with DYNA3D and ParaDyn. *Phys. Status Solidi (B)* **2005**, *242*, 585–594. [CrossRef]
31. Lakes, R.; Wojciechowski, K.W. Negative compressibility, negative Poisson's ratio, and stability. *Phys. Status Solidi (B)* **2008**, *245*, 545–551. [CrossRef]
32. Grima, J.N.; Winczewski, S.; Mizzi, L.; Grech, M.C.; Cauchi, R.; Gatt, R.; Attard, D.; Wojciechowski, K.W.; Rybicki, J. Tailoring graphene to achieve negative Poisson's ratio properties. *Adv. Mater.* **2015**, *27*, 1455–1459. [CrossRef]
33. Poźniak, A.A.; Wojciechowski, K.W.; Grima, J.N.; Mizzi, L. Planar auxeticity from elliptic inclusions. *Compos. Part B Eng.* **2016**, *94*, 379–388. [CrossRef]
34. Narojczyk, J.W.; Wojciechowski, K.W.; Smardzewski, J.; Imre, A.R.; Grima, J.N.; Bilski, M. Cancellation of Auxetic Properties in F.C.C. Hard Sphere Crystals by Hybrid Layer-Channel Nanoinclusions Filled by Hard Spheres of Another Diameter. *Materials* **2021**, *14*, 3008. [CrossRef] [PubMed]
35. Grima, J.N.; Evans, K.E. Auxetic behavior from rotating squares. *J. Mater. Sci. Lett.* **2000**, *19*, 1563–1565. [CrossRef]
36. Francesconi, L.; Taylor, M.; Bertoldi, K.; Baldi, A. Static and modal analysis of low porosity thin metallic auxetic structures using speckle interferometry and digital image correlation. *Exp. Mech.* **2018**, *58*, 283–300. [CrossRef]
37. Du, Z.; Zhou, M.; Liu, H.; He, L. Study on negative Poisson's ratio of auxetic yarn under tension: Part 1–Theoretical analysis. *Text. Res. J.* **2015**, *85*, 487–498. [CrossRef]
38. Jiang, L.; Gu, B.; Hu, H. Auxetic composite made with multilayer orthogonal structural reinforcement. *Compos. Struct.* **2016**, *135*, 23–29. [CrossRef]
39. Gao, R.; Li, D.; Dong, L.; Wang, X. Numerical analysis of the mechanical properties of 3D random Voronoi structures with negative Poisson's ratio. *Phys. Status Solidi (B)* **2019**, *256*, 1800539. [CrossRef]
40. Ren, C.; Yang, D.; Qin, H. Mechanical performance of multidirectional buckling-based negative stiffness metamaterials: An analytical and numerical study. *Materials* **2018**, *11*, 1078. [CrossRef]
41. Jiang, L.; Hu, H. Low-velocity impact response of multilayer orthogonal structural composite with auxetic effect. *Compos. Struct.* **2017**, *169*, 62–68. [CrossRef]
42. Zhou, L.; Zeng, J.; Jiang, L.; Hu, H. Low-velocity impact properties of 3D auxetic textile composite. *J. Mater. Sci.* **2018**, *53*, 3899–3914. [CrossRef]
43. Lakes, R. Foam structures with a negative Poisson's ratio. *Science* **1987**, *235*, 1038–1040. [CrossRef] [PubMed]
44. Choi, J.; Lakes, R. Non-linear properties of metallic cellular materials with a negative Poisson's ratio. *J. Mater. Sci.* **1992**, *27*, 5375–5381. [CrossRef]
45. Masters, I.; Evans, K. Models for the elastic deformation of honeycombs. *Compos. Struct.* **1996**, *35*, 403–422. [CrossRef]
46. Grima, J.N.; Gatt, R.; Farrugia, P.S. On the properties of auxetic meta-tetrachiral structures. *Phys. Status Solidi (B)* **2008**, *245*, 511–520. [CrossRef]
47. Spadoni, A.; Ruzzene, M. Elasto-static micropolar behavior of a chiral auxetic lattice. *J. Mech. Phys. Solids* **2012**, *60*, 156–171. [CrossRef]
48. Jiang, Y.; Li, Y. 3D printed chiral cellular solids with amplified auxetic effects due to elevated internal rotation. *Adv. Eng. Mater.* **2017**, *19*, 1600609. [CrossRef]
49. Wojciechowski, K.W. Two-dimensional isotropic system with a negative poisson ratio. *Phys. Lett. A* **1989**, *137*, 60–64. [CrossRef]
50. Wojciechowski, K.W. Non-chiral, molecular model of negative Poisson ratio in two dimensions. *J. Phys. A Math. Gen.* **2003**, *36*, 11765. [CrossRef]
51. Prall, D.; Lakes, R. Properties of a chiral honeycomb with a Poisson's ratio of—1. *Int. J. Mech. Sci.* **1997**, *39*, 305–314. [CrossRef]
52. Alderson, A.; Alderson, K.L.; Attard, D.; Evans, K.E.; Gatt, R.; Grima, J.N.; Miller, W.; Ravirala, N.; Smith, C.W.; Zied, K. Elastic constants of 3-, 4-and 6-connected chiral and anti-chiral honeycombs subject to uniaxial in-plane loading. *Compos. Sci. Technol.* **2010**, *70*, 1042–1048. [CrossRef]

53. Idczak, E.; Strek, T. Minimization of Poisson's ratio in anti-tetra-chiral two-phase structure. *IOP Conf. Ser. Mater. Sci. Eng.* **2017**, *248*, 012006. [CrossRef]
54. Zhang, H.; Luo, Y.; Kang, Z. Bi-material microstructural design of chiral auxetic metamaterials using topology optimization. *Compos. Struct.* **2018**, *195*, 232–248. [CrossRef]
55. Jiang, Y.; Li, Y. Novel 3D-printed hybrid auxetic mechanical metamaterial with chirality-induced sequential cell opening mechanisms. *Adv. Eng. Mater.* **2018**, *20*, 1700744. [CrossRef]
56. Mizzi, L.; Mahdi, E.; Titov, K.; Gatt, R.; Attard, D.; Evans, K.; Grima, J.; Tan, J. Mechanical metamaterials with star-shaped pores exhibiting negative and zero Poisson's ratio. *Mater. Des.* **2018**, *146*, 28–37. [CrossRef]
57. Chen, Z.; Wu, X.; Xie, Y.M.; Wang, Z.; Zhou, S. Re-entrant auxetic lattices with enhanced stiffness: A numerical study. *Int. J. Mech. Sci.* **2020**, *178*, 105619. [CrossRef]
58. Ng, C.K.; Saxena, K.K.; Das, R.; Flores, E.I. On the anisotropic and negative thermal expansion from dual-material re-entrant-type cellular metamaterials. *J. Mater. Sci.* **2017**, *52*, 899–912. [CrossRef]
59. Xiao, D.; Kang, X.; Li, Y.; Wu, W.; Lu, J.; Zhao, G.; Fang, D. Insight into the negative Poisson's ratio effect of metallic auxetic reentrant honeycomb under dynamic compression. *Mater. Sci. Eng. A Struct. Mater. Prop. Microstruct. Process.* **2019**, *763*, 138151. [CrossRef]
60. Pozniak, A.A.; Wojciechowski, K.W. Poisson's ratio of rectangular anti-chiral structures with size dispersion of circular nodes. *Phys. Status Solidi (B)* **2014**, *251*, 367–374. [CrossRef]
61. Strek, T.; Jopek, H.; Wojciechowski, K.W. The influence of large deformations on mechanical properties of sinusoidal ligament structures. *Smart Mater. Struct.* **2016**, *25*, 054002. [CrossRef]
62. Tabacu, S.; Badea, A.; Sandu, A. Complex Analysis of an Auxetic Structure under Compressive Loads. *Sustainability* **2023**, *15*, 6805. [CrossRef]
63. Tretiakov, K.V. Negative Poisson's ratio of two-dimensional hard cyclic tetramers. *J. Non Cryst. Solids* **2009**, *355*, 1435–1438. [CrossRef]
64. Tretiakov, K.V.; Wojciechowski, K.W. Auxetic, Partially Auxetic, and Nonauxetic Behaviour in 2D Crystals of Hard Cyclic Tetramers. *Phys. Status Solidi (RRL) Rapid Res. Lett.* **2020**, *14*, 2000198. [CrossRef]
65. Tretiakov, K.V.; Wojciechowski, K.W. Auxeticity and Its Pressure Dependence for Strongly Anisotropic Hard Cyclic Tetramers. *Phys. Status Solidi (RRL) Rapid Res. Lett.* **2022**, *16*, 2200288. [CrossRef]
66. Lim, T.-C. An Auxetic Metamaterial Based on Rotating and Nonrotating Rigid Units Inspired by an Aztec Geometric Pattern. *Phys. Status Solidi (B)* **2022**, *259*, 2200385. [CrossRef]
67. Lim, T.-C. Auxetic and non-auxetic metamaterial model from interconnected rotating parallelograms and triangles. *Phys. Status Solidi (B)* **2023**. (ahead of pub). [CrossRef]
68. Narojczyk, J.W.; Wojciechowski, K.W.; Tretiakov, K.V.; Smardzewski, J.; Scarpa, F.; Piglowski, P.M.; Kowalik, M.; Imre, A.R.; Bilski, M. Auxetic Properties of a f.c.c. Crystal of Hard Spheres with an Array of [001]-Nanochannels Filled by Hard Spheres of Another Diameter. *Phys. Status Solidi (B)* **2019**, *256*, 1800611. [CrossRef]
69. Narojczyk, J.W. The f.c.c. Crystals of Hard Spheres with an Array of [001]-Nanochannel Inclusions Filled by the Simplest Hard Sphere Molecules. *Comput. Methods Sci. Technol.* **2023**, *29*, 37–44. [CrossRef]
70. Gaspar, N.; Ren, X.J.; Smith, C.W.; Grima, J.N.; Evans, K.E. Novel honeycombs with auxetic behaviour. *Acta Mater.* **2005**, *53*, 2439–2445. [CrossRef]